Light-Triggered Anti-ambipolar Transistor Based on an In-Plane Lateral Homojunction

Hecheng Han, Baoqing Zhang, Zihao Zhang, Yiming Wang, Chuan Liu, Arun Kumar Singh, Aimin Song, Yuxiang Li,* Jidong Jin,* and Jiawei Zhang*

Cite This: *Nano Lett.* 2024, 24, 8602−8608

Read Online

ACCESS | Metrics & More | Article Recommendations | Supporting Information

ABSTRACT: Currently, the construction of anti-ambipolar transistors (AATs) is primarily based on asymmetric heterostructures, which are challenging to fabricate. AATs used for photodetection are accompanied by dark currents that prove difficult to suppress, resulting in reduced sensitivity. This work presents light-triggered AATs based on an in-plane lateral WSe_2 homojunction without van der Waals heterostructures. In this device, the WSe_2 channel is partially electrically controlled by the back gate due to the screening effect of the bottom electrode, resulting in a homojunction that is dynamically modulated with gate voltage, exhibiting electrostatically reconfigurable and light-triggered anti-ambipolar behaviors. It exhibits high responsivity (188 A/W) and detectivity (8.94×10^{14} Jones) under 635 nm illumination with a low power density of 0.23 $\mu W/cm^2$, promising a new approach to low-power, high-performance photodetectors. Moreover, the device demonstrates efficient self-driven photodetection. Furthermore, ternary inverters are realized using monolithic WSe_2, simplifying the manufacturing of multivalued logic devices.

KEYWORDS: weak light detection, asymmetric structure, self-driven photodetection, light-triggered anti-ambipolar transistors
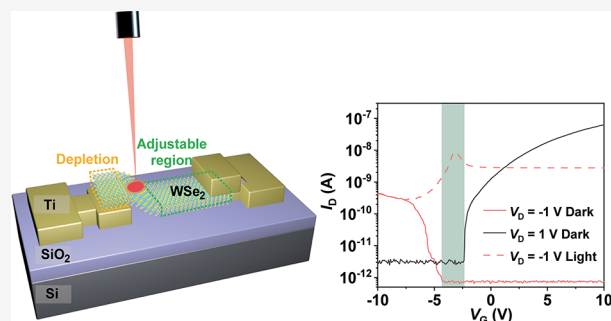
Distinctly different from unipolar field-effect transistors and conventional ambipolar devices, anti-ambipolar transistors (AATs) are devices that exhibit a convex-shaped transfer characteristic, where the channel electrical conductance peaks at a specific gate bias.[1,2] Typically, AATs are based on asymmetric device structures in which n-type and p-type semiconductors are located at both ends, creating a p-n heterojunction at the middle overlapping part.[1,2] Particularly, the turn-on voltage of a p-type semiconductor needs to be larger than that of the n-type counterpart.[1–3] It is generally assumed that the spike-shaped transient current of AATs occurs when both p- and n-channels in series are simultaneously in the on-state.[1–3] Hence, the design of AATs requires carefully matched turn-on voltages for the p/n-type semiconductors, precisely controlled carrier density, and elaborate energy band alignment.[1,2] Currently, researchers have developed many outstanding AATs, including MoS_2/$MoTe_2$,[4,5] 1D GaAsSb/2D MoS_2,[3] InSe/WSe_2,[6] $MoTe_2$/SnS_2,[7] and more. In fact, this anti-ambipolar characteristic has crucial applications in logic circuits, optoelectronics, and quantum superposition state processing.[1–3,8,9] For instance, by utilizing the flipping of transconductance, these devices can be applied to construct frequency doublers, binary phase-shift keying, and ternary inverters.[1–3] Additionally, recent studies have found that light can act as a switch to realize the device conversion between binary and multivalued logic (MVL), providing a new

paradigm for information encryption.[4] Additionally to the aforementioned features, adjusting the different energy band alignments within the heterojunction through gate control enables the manipulation of the separation and transport of photoinduced carriers, enabling optimization of photocurrent amplitude.[3,4] This characteristic can be utilized for the effective capture of optical signals.[3,4]

By constructing AATs based on heterojunctions, researchers have successfully employed a gate-controlled modulation strategy to achieve effective acquisition of optical signals.[3,4] However, these photodetectors operate when both p-type and n-type semiconductors conduct simultaneously, making the carrier concentration of these gate-tunable photodetectors largely subject to gate control rather than the optical signal.[3,4] This is bound to result in higher dark current and consequently high power consumption, thereby reducing detectivity and the ability to capture weak optical signals. Achieving both the off state (dark condition) and the light-triggered anti-ambipolar state with the same gate modulation can enhance weak optical
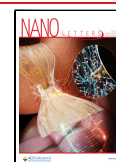
signal detection. Nevertheless, studies of light-triggered anti-ambipolar transistors with extremely low dark current remain limited. This may result from the challenging fabrication of anti-ambipolar heterodiodes and the lack of effective light-triggered anti-ambipolar transistor fabrication strategies.[3]

In existing methods, AATs are constructed based on heterojunctions, requiring sophisticated transfer techniques.[4−6] Unfortunately, precise transfers entail a certain risk of failure, increased operational complexity and time costs.[10−12] More-over, the band structure of two-dimensional (2D) materials changes significantly with layer count, requiring precise identification techniques.[13,14] In principle, the energy bands of both the p/n-type semiconductors and the intermediate heterojunction change simultaneously under gate modula-tion.[4−6] Furthermore, when irradiation is introduced, it is almost impossible to ascertain the principles.[3,15] Indeed, the principles guiding conventional AATs are controversial, while the physical principles of light-triggered anti-ambipolar transistors are even more intricate.[3,4] Therefore, there is a need to develop structurally optimized AATs without van der Waals (vdW) heterojunctions to simplify fabrication and address theoretical research challenges.[3]

This work presents the demonstration of light-triggered WSe$_2$ AATs without vdW heterostructures, for the con-struction of highly sensitive photodetectors. In this device, the WSe$_2$ channel can be divided into two regions: either modulated or unmodulated by the back gate through the screening effect of the bottom metal electrode. The built-in electric field direction of WSe$_2$ AATs changes with the variation of gate voltage (V_G) due to unilateral electrical control of the back gate, exhibiting electrostatically reconfig-urable and light-triggered anti-ambipolar transport behaviors. It is worth noting that the WSe$_2$ AATs achieve low dark current (0.69 pA) and a sensitive response to light due to phototriggered anti-ambipolar transport occurring in the depletion region (dark condition). The device exhibits high responsivity (188 A/W) and detectivity (8.94 × 10^{14} Jones) under 635 nm illumination with a weak power density of 0.23 μW/cm^2. Additionally, an extremely high responsivity of 1.97 × 10^{11} V/W can be realized with very low power consumption (0.412 nW) through WSe$_2$ AATs connected to an external resistor. Moreover, WSe$_2$ AATs with asymmetric electrodes exhibit excellent self-driven photodetection performance, with a high responsivity of 20.2 A/W and a detectivity of 2.1 × 10^{13} Jones. Therefore, the presented device structure has diverse application prospects in low-power photodetection. Finally, ternary inverters are fabricated using a monolithic WSe$_2$, significantly simplifying the manufacturing of MVL circuits.

Figure 1a illustrates the schematic structure of a WSe$_2$ AAT. The fabrication method for the WSe$_2$ AAT device is detailed in section 1 of the Supporting Information. The Raman spectrum shown in Figure S1 reveals a peak difference of 10 cm^{-1} between the E$_{2g}^1$ and A$_{1g}$ vibration modes of WSe$_2$, indicating that the channel material in the device is multilayer WSe$_2$.[16,17] In the WSe$_2$ AAT, the WSe$_2$ region on SiO$_2$ can be modulated by electrical control of the back gate, while the WSe$_2$ region on Ti is only weakly modulated due to the screening effect of the bottom electrode.[18] Figure 1b shows the top view of a WSe$_2$ AAT. Figure 1c illustrates the transfer curve (I_D−V_G at V_D = −1 V) of the WSe$_2$ AAT when illuminated with a 635 nm light source, revealing a distinct convex-shaped anti-ambipolar transfer characteristic. Within the green shaded region, the WSe$_2$ AAT shows a decrease in drain current in the negative
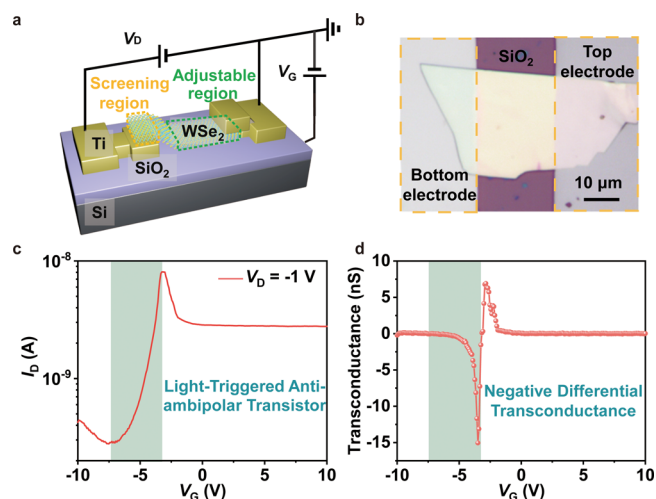

Figure 1. Device structure and transfer characteristics of the WSe$_2$ AAT. (a) Schematic of the WSe$_2$ AAT. (b) Optical image of the WSe$_2$ AAT. (c) I_D−V_G curve of the WSe$_2$ AAT under illumination (λ of 635 nm and power density of 20.61 μW/cm^2). (d) g_m−V_G curve of the WSe$_2$ AAT under illumination (λ of 635 nm and power density of 20.61 μW/cm^2).

V_G direction under illumination. The peak-to-valley ratio of our device is 29.3 under 635 nm light illumination with a power density of 20.61 μW/cm^2, which is comparable to that of previously reported devices based on two-dimensional materials.[19−24] Moreover, a comparable anti-ambipolar transfer characteristic is evident when applying drain voltages of V_D = −0.5 V, −1 V, −1.5 and 1 V (detailed device electrical properties can be found in section 2 of the Supporting Information). The corresponding transconductance (g_m) with respect to the V_G under illumination is shown in Figure 1d, where negative differential transconductance can be clearly observed.

To investigate the distinctive phenomena exhibited by this device, a series of electrical tests were conducted under both dark and light illumination conditions. The transfer curve of the device under dark conditions demonstrates that the device polarity can be reconfigured as either p-type or n-type when the drain bias is set at −1 or 1 V respectively, as illustrated in Figure 2a. The device's dark current was 0.69 pA, with on/off current ratios for both n- and p-type transistors approximately equal to 10^3. The green shaded region in Figure 2a consistently remains in the off state, regardless of whether a positive or negative drain bias is applied. Moreover, the light-triggered anti-ambipolar transport behavior precisely occurs in this green-shaded region when a negative drain bias (V_D = −1 V) is applied. This phenomenon is quite different from the previous research, where anti-ambipolar transport behavior typically occurs when both p- and n-channels are simultaneously in the on-state.[3,25] The reconfigurable transfer behavior of this device can be attributed to the in-plane homojunction, which undergoes changes in response to variations in V_G.[18] The homojunction effectively blocks the injection of charge carriers from the bottom electrode,[18] while holes and electrons can be injected from the top electrode by tunneling through narrow Schottky barrier.[18,26,27] Therefore, this WSe$_2$ AAT exhibits reconfigurable transfer behavior in the dark, and its direction can be determined by V_G. For detailed energy band diagrams and the I_D-V_D curve of the device without illumination, please refer to section 3 of the Supporting Information.
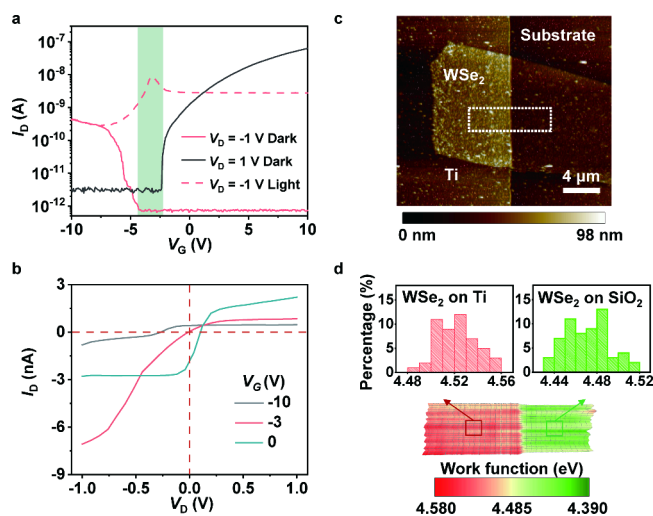
Figure 2. Formation of the in-plane homojunction. (a) I_D-V_G curves of the WSe$_2$ AAT under dark and light illumination (λ of 635 nm and power density of 20.61 μW/cm^2). (b) I_D-V_D curves of the WSe$_2$ AAT under illumination (λ of 635 nm and power density of 20.61 μW/cm^2). (c) Partial AFM image of the WSe$_2$ AAT. The dotted square blocks indicate the KPFM mapping area. (d) KPFM mapping image and work function histograms of the dotted square blocks in panel c.

Figure 2b illustrates the I_D-V_D characteristics of the WSe$_2$ AAT under 635 nm illumination (power density = 20.61 μW/cm^2). As V_G changes from −10 to 0 V, both the short-circuit current (I_{sc}) and open-circuit voltage (V_{oc}) of the AAT undergo changes in sign, indicating a change in the polarity of the built-in electric field.[28,29] At $V_G = -3$ V, it is notable that there are minimal photovoltaic effects, suggesting the absence

of a significant built-in electric field.[28,29] This suggests that modulation of V_G may align the energy bands of two regions: WSe$_2$ on the Ti bottom electrode and WSe$_2$ on SiO$_2$, leading to the occurrence of light-triggered anti-ambipolar transport behaviors. Whether V_G is increased or decreased, a homojunction is generated in the boundary between the two regions, resulting in a decrease in photocurrent. Thus, we preliminarily infer that these unique phenomena may be attributed to the dynamically modulated homojunction with the back gate. The Fermi level (E_F) of 2D materials can be determined using $E_F = \hbar v_F \sqrt{n}$, where $\hbar$ is the reduced Planck constant, n is the carrier concentration, and v_F is the Fermi velocity (5.0×10^5 m/s in WSe$_2$).[30,31] When the V_G changes from zero to −3 V, the calculated E_F shift is −82.8 meV. Since the WSe$_2$ located on the bottom Ti electrode is not subject to gate modulation, its E_F can be considered constant. Thus, at zero gate voltage, the difference in E_F between the two regions is approximately 82.8 meV. The existence of the in-plane homojunction was further confirmed using Kelvin probe force microscopy (KPFM). The partial atomic force microscopy (AFM) image of the WSe$_2$ anti-ambipolar transistor is shown in Figure 2c. The work functions of WSe$_2$ in the highlighted region in Figure 2c were determined by measuring the contact potential difference (ΔV_{CPD}) between the KPFM tip (Φ_{Tip}) and WSe$_2$ film (Φ_S), and then subtracting ΔV_{CPD} from Φ_{Tip} ($\Phi_S = \Phi_{Tip} - \Delta V_{CPD}$).[19] Figure 2d shows KPFM mapping image and corresponding regional work-function histograms. The average work functions were 4.55 eV for WSe$_2$ on Ti and 4.47 eV for WSe$_2$ on SiO$_2$ regions, which aligns with the calculation results. This difference in work function of WSe$_2$ on different regions could be attributed to the construction of asymmetric electrodes.[32,33] The measured thickness of the WSe$_2$ nanosheet and the Ti electrode in the device, along with
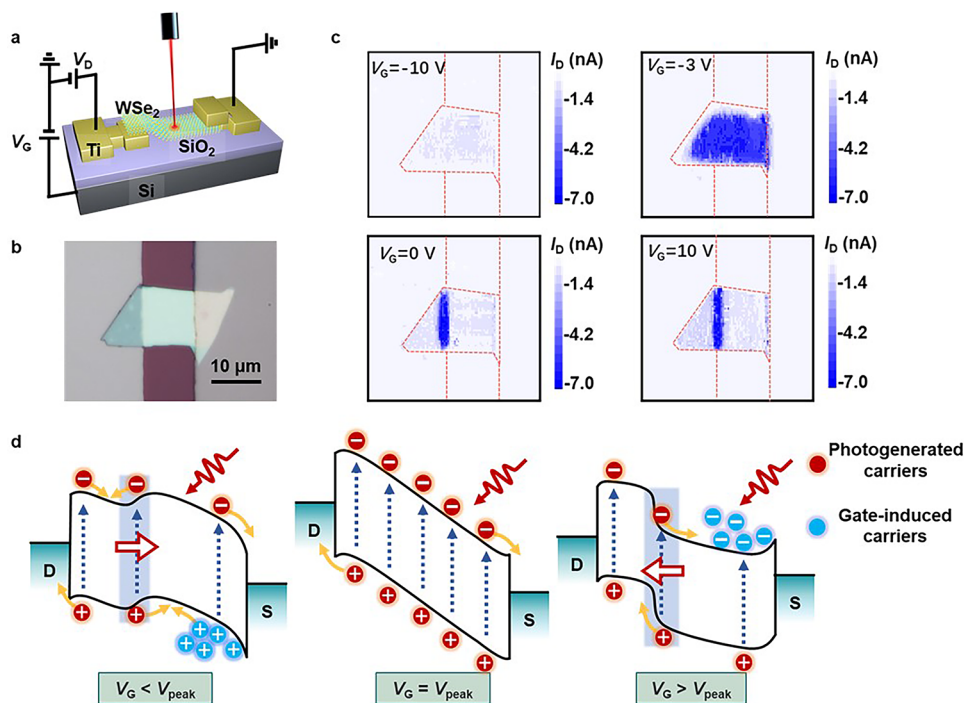

Figure 3. Mechanism of anti-ambipolar transport behavior. (a) Experimental setup for obtaining SPCM images of the WSe$_2$ AAT. (b) Top-view optical image of the WSe$_2$ AAT for SPCM measurements. (c) SPCM images of the WSe$_2$ AAT at different gate voltages with a V_D of −1 V. (d) Energy-band diagrams of WSe$_2$ AAT under light illumination. Red and blue circles indicate photogenerated carriers and gate-induced carriers, respectively.

a plausible explanation of the formation of in-plane homojunction, can be found in section 3 of the Supporting Information.

To validate the operational mechanism of the WSe$_2$ AAT, scanning photocurrent microscopy (SPCM) images were acquired by utilizing a focused laser beam to scan the device and record the induced photocurrent. The experimental set up for obtaining SPCM images of the WSe$_2$ AAT is depicted in Figure 3a. The top-view optical image of the WSe$_2$ AAT for SPCM measurements is depicted in Figure 3b. Figure 3c presents SPCM images of the WSe$_2$ AAT under different gate voltages, revealing distinct photocurrent distributions. At V_G = −10 V, minimal photocurrent is observed across the transistor. At V_G = −3 V, the photocurrent almost covers the entire transistor, whereas at V_G = 0 or 10 V, the photocurrent is mainly generated at the Ti bottom electrode edge covered by WSe$_2$. Based on the above phenomena, the principle of the light-triggered anti-ambipolar transistor is depicted in the Figure 3d. Carriers in the light-triggered WSe$_2$ AAT are divided into photogenerated and gate-induced, represented by red and blue circles in Figure 3d. Anti-ambipolar transport occurs when p- and n-channel are simultaneously in off-state. Consequently, a state exists in which the energy bands of WSe$_2$ on Ti and SiO$_2$ align, resulting in a very low carrier density in the channel. This state can be considered as a depletion state, leading to an off-state in the dark. However, an external light source can effectively enhance the production of photogenerated electrons and holes, simultaneously separating them under the applied bias voltage, resulting in a significant current signal.[19] At this point, photogenerated electrons and holes jointly dominate anti-ambipolar transport, leading to the peak photocurrent. This inflection point is marked by $V_G = V_{peak}$. When $V_G < V_{peak}$, electrostatic doping induced by the gate potential shifts the E_F of WSe$_2$ on SiO$_2$ downward, increasing holes in the channel.[34] The direction of the built-in electric field is opposite to the direction of the applied bias.[34] The photocurrent induced by drain bias is offset by the photogenerated carriers within the homojunction.[19] Moreover, increasing V_G intensifies the built-in electric field. Consequently, the requirement for the drain bias to overcome the built-in electric field increases, resulting in a significant drop in current. When $V_G > V_{peak}$, the E_F of WSe$_2$ on SiO$_2$ upshifts, and the photocurrent is dominated by the built-in electric field due to the same direction of the built-in electric field and the drain bias. The channel area on SiO$_2$, which occupies a significantly larger area, makes a weak contribution to the current, resulting in a decrease in the overall current. Thus, the transformation of the built-in electric field, controlled by the unilateral back gate, is the key factor causing light-triggered anti-ambipolar transport behavior.

To evaluate self-powered photodetection performances of the WSe$_2$ AATs with asymmetric electrode structures, various photoelectric characterizations were conducted under 635 nm illumination, as illustrated in Figure 4. Figure 4a shows the I_D−V_D curves of the WSe$_2$ AAT under dark and light conditions with variable incident flux. As the light power density increases from 8.21 μW/cm^2 to 28.72 μW/cm^2, there is an increase in both the I_{sc} and V_{oc}. Figure 4b illustrates the time-dependent properties of the WSe$_2$ AAT under different light power densities, showing consistent and stable photoelectric signals, which highlight the device's robustness. Figure 4c depicts the photoresponse waveform of the WSe$_2$ AAT as measured by oscilloscope, revealing a fast photoresponse with a rising time
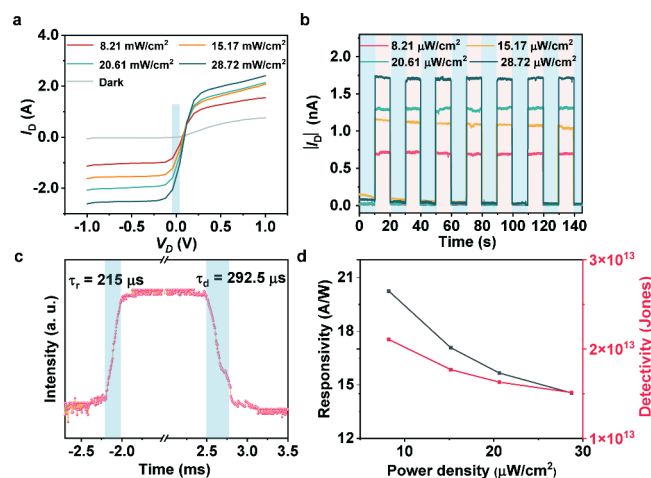

Figure 4. Self-powered photoelectric detection performance of the WSe$_2$ AAT with an asymmetric electrode architecture. (a) I_D−V_D curves of the WSe$_2$ AAT under dark and laser illumination (λ of 635 nm) with various power densities. (b) Time-dependent photoresponse properties of the WSe$_2$ AAT under laser illumination (λ of 635 nm) with various power densities. (c) Photoresponse waveform of the WSe$_2$ AAT captured on the oscilloscope. (d) Responsivity (black squares) and detectivity (red squares) of the WSe$_2$ AAT as a function of illumination intensity.

of 215 μs and a decay time of 292.5 μs. The calculation of the photodetector device performance parameters is provided in section 4 of the Supporting Information. The responsivity and detectivity of the device decreases with increasing incident light power, as depicted in Figure 4d. Notably, at 8.21 μW/cm^2, the device demonstrates a high responsivity of 20.2 A/W and detectivity of 2.1 × 10^{13} Jones. Overall, the responsivity and detectivity of our device are comparable to or improve upon those of other self-driven photodetectors based on 2D materials (see Table S1). These findings highlight the potential of the WSe$_2$ AATs as efficient photodetectors.

When very weak light is used (e.g., 1.51 μW/cm^2) to measure the self-driven photocurrent of the WSe$_2$ AAT, the resulting self-driven photocurrent becomes extremely small (see Figure S7). Despite this, anti-ambipolar transport persists when the device is illuminated with weak light at power densities ranging from 0.23 to 2.88 μW/cm^2, as shown in Figure 5a. The high sensitivity of the WSe$_2$ AAT to weak light can be attributed to the following main factors. First, the device exhibits low dark current in the pA range, thereby demonstrating high sensitivity,[35−43] as depicted in the inset of Figure 5a. Second, when light-triggered anti-ambipolar transport occurs, the entire WSe$_2$ channel serves as a photosensitive area. Furthermore, the WSe$_2$ AAT demonstrates a strong correlation between peak-to-valley ratio and light intensity (see Figure S8a). Due to this strong correlation, it can be utilized in various applications, including photodetection, circuit logic, and information encryption.[3,4] Figure 5b illustrates consistent and stable time-dependent properties of the WSe$_2$ AAT under variable weak light illumination. As depicted in Figure 5c, the responsivity and detectivity of the WSe$_2$ AAT show a decreasing trend with increasing light power density in the range of 0.23 to 2.88 μW/cm^2. The R^2 value of the linear fit for both responsivity and detectivity in Figure 5c is 0.9916, indicating excellent linearity. Notably, the device demonstrates a very high responsivity of 188 A/W and detectivity of 8.94 × 10^{14} Jones at an incident light power of
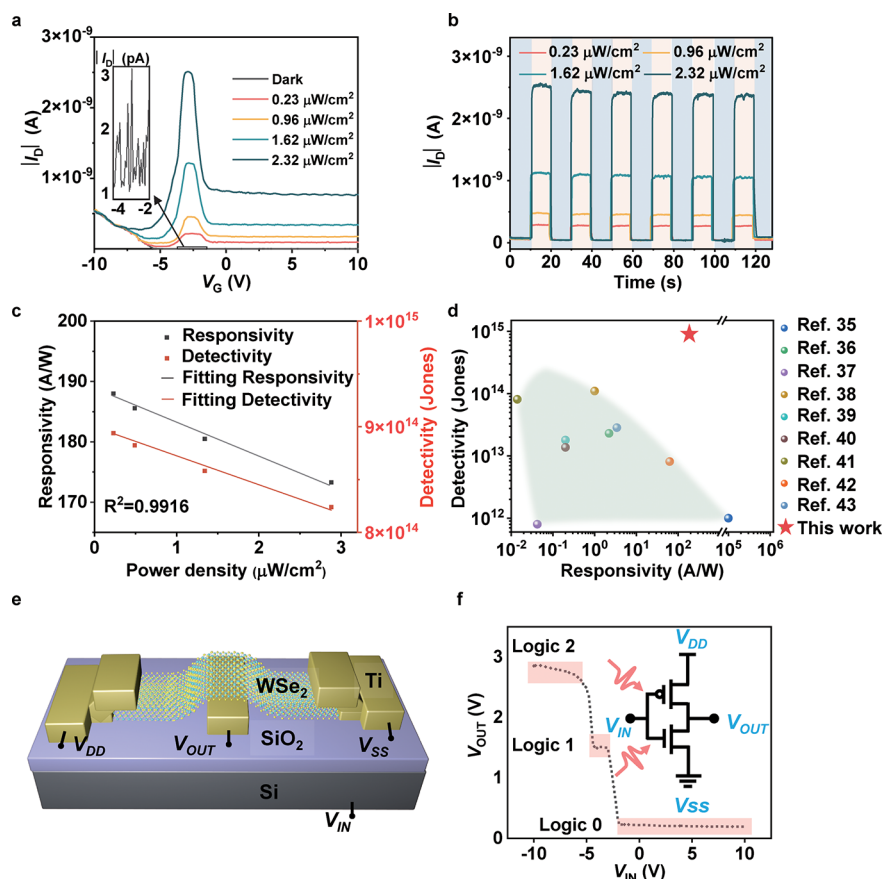
Figure 5. Weak light detection and ternary Inverter. (a) I_D-V_G curves of the WSe$_2$ AAT under dark and light illumination (λ of 635 nm) at different power densities (0.23–2.88 μW/cm^2). The inset shows a close-up of the I_D-V_G curve of the WSe$_2$ AAT under dark conditions when -4 V $< V_G < -2$ V. (b) Time-dependent photoresponse properties of the WSe$_2$ AAT under light illumination (λ of 635 nm) at different power densities (0.23–2.88 μW/cm^2). (c) Responsivity and detectivity of the WSe$_2$ AAT as a function of power density ranging from 0.23 to 2.88 μW/cm^2. (d) Summary of performance metrics for weak light detectors. (e) Schematic of the WSe$_2$ ternary inverter. (f) Voltage-transfer characteristics of the ternary inverter (V_{DD} = 3 V).

0.23 μW/cm^2. A comparison with previously reported weak light detectors is presented in Figure 5d. Our WSe$_2$ AAT demonstrates comparable to or even better responsivity and detectivity compared to those of previously reported weak light detectors[36–43] (see Table S2).

To improve weak light response and reduce power consumption, a resistor was integrated with the WSe$_2$ AAT to create a circuit, as shown in Figure S8b (detailed test results of the circuit are available in section 5 of the Supporting Information). The circuit exhibits a very high responsivity of 1.97×10^{11} V/W at 0.23 μW/cm^2 (see Figure S8d), surpassing that of typical weak light photodetector. Moreover, the circuit's power consumption is remarkably low, measured at 0.412 nW (see Figure S8e), indicating a promising new approach for low-power, high-sensitivity photodetectors. Finally, a ternary inverter was constructed using monolithic WSe$_2$ and its schematic diagram is shown in Figure 5e. Figure 5f shows the voltage-transfer characteristics of the ternary inverter under laser illumination (λ = 635 nm, power density = 2.61 μW/cm^2) when V$_{DD}$ equals 3 V, with the inset displaying the circuit diagram of the ternary inverter. The inverter achieved three distinct states: an intermediate value (logic state "1"), as well as high (logic state "2") and low (logic state "0") voltage values (More detailed information on the light-triggered ternary inverter is presented in section 6 of the Supporting

Information). This ternary inverter can significantly simplify the manufacturing challenges associated with MVL circuits.

In conclusion, we have demonstrated a light-triggered AAT based on in-plane lateral WSe$_2$ homojunctions, diverging from the use of established vdW heterostructure design. Our findings reveal a unique light-triggered anti-ambipolar transport phenomenon distinct from previous systems, wherein spike-shaped currents occur when both p- and n-channels are simultaneously in the on-state. Through the screening effect of the bottom electrode, the WSe$_2$ channel on substrate, rather than the bottom electrode, is electrically controlled by the back gate, resulting in a homojunction dynamically modulated with V_G. This V_G modulation can align the energy band of WSe$_2$ in two regions (modulated or unmodulated region), leading to light-triggered anti-ambipolar behavior. Upon increase or decrease of V_G, a homogeneous junction is generated at the boundary, thereby decreasing photocurrent. The WSe$_2$ AAT exhibits low dark current (0.69 pA) and a sensitive response to light due to phototriggered anti-ambipolar transport occurring in the depletion region (dark condition). It demonstrates high responsivity (188 A/W) and detectivity (8.94×10^{14} Jones) under 635 nm illumination with a weak power density of 0.23 μW/cm^2, offering a new approach to high-performance photodetectors. Additionally, this asymmetrical architecture also holds the potential to facilitate advances in self-power photodetection and multivalued logic circuits.

ASSOCIATED CONTENT

ⓈⒾ Supporting Information

The Supporting Information is available free of charge at https://pubs.acs.org/doi/10.1021/acs.nanolett.4c01679.

Additional information about methods, transfer characteristics of the WSe_2 AAT at different voltages, formation of the in-plane homojunction, self-powered photoelectric performance, weak light detection performance, and light-triggered ternary inverter (PDF)

AUTHOR INFORMATION

Corresponding Authors

Yuxiang Li − *Shandong Technology Center of Nanodevices and Integration, School of Integrated Circuit, Shandong University, Jinan 250101, China;* ⓘ orcid.org/0000-0002-9457-769X; Email: yxli@sdu.edu.cn

Jidong Jin − *Department of Photonics and Nanoelectronics, Hanyang University, Ansan 15588, Republic of Korea;* ⓘ orcid.org/0000-0002-8400-0053; Email: jinjidong@hanyang.ac.kr

Jiawei Zhang − *Shandong Technology Center of Nanodevices and Integration, School of Integrated Circuit, Shandong University, Jinan 250101, China;* ⓘ orcid.org/0000-0002-1624-9535; Email: Jiawei.zhang@sdu.edu.cn

Authors

Hecheng Han − *Shandong Technology Center of Nanodevices and Integration, School of Integrated Circuit, Shandong University, Jinan 250101, China*

Baoqing Zhang − *Shandong Technology Center of Nanodevices and Integration, School of Integrated Circuit, Shandong University, Jinan 250101, China*

Zihao Zhang − *Shandong Technology Center of Nanodevices and Integration, School of Integrated Circuit, Shandong University, Jinan 250101, China*

Yiming Wang − *Shandong Technology Center of Nanodevices and Integration, School of Integrated Circuit, Shandong University, Jinan 250101, China*

Chuan Liu − *State Key Laboratory of Optoelectronic Materials and Technologies, Guangdong Province Key Laboratory of Display Material and Technology, School of Electronics and Information Technology, Sun Yat-Sen University, Guangzhou 510275, China;* ⓘ orcid.org/0000-0002-0695-592X

Arun Kumar Singh − *Department of Electronics and Communications Engineering, Punjab Engineering College (Deemed to be University), Chandigarh 160012, India*

Aimin Song − *Department of Electrical and Electronic Engineering, University of Manchester, Manchester M13 9PL, United Kingdom; Institute of Nanoscience and Applications, Southern University of Science and Technology, Shenzhen 518055, China;* ⓘ orcid.org/0000-0001-6550-518X

Complete contact information is available at:
https://pubs.acs.org/10.1021/acs.nanolett.4c01679

Author Contributions

Y.L., J.J., and J.Z. proposed and supervised the study. H.H. performed the device fabrication and characterization. B.Z., Z.Z., and Y.W. assisted with the electrical measurements. C.L., A.K.S., and A.S. assisted with data analysis. H.H. and J.J. wrote the manuscript. All of the authors discussed the results and commented on the manuscript.

Notes

The authors declare no competing financial interest.

ACKNOWLEDGMENTS

REFERENCES

(1) Kwon, J.; Shin, J.-C.; Ryu, H.; Lee, J. Y.; Seo, D.; Watanabe, K.; Taniguchi, T.; Kim, Y. D.; Hone, J.; Lee, C.-H.; Lee, G.-H. Multioperation-Mode Light-Emitting Field-Effect Transistors Based on van der Waals Heterostructure. *Adv. Mater.* **2020**, *32* (43), No. 2003567.

(2) Meng, Y.; Wang, W.; Wang, W.; Li, B.; Zhang, Y.; Ho, J. Anti-Ambipolar Heterojunctions: Materials, Devices, and Circuits. *Adv. Mater.* **2024**, *36*, No. 2306290.

(3) Wang, W.; Wang, W.; Meng, Y.; Quan, Q.; Lai, Z.; Li, D.; Xie, P.; Yip, S.; Kang, X.; Bu, X.; Chen, D.; Liu, C.; Ho, J. C. Mixed-Dimensional Anti-ambipolar Phototransistors Based on 1D GaAsSb/2D MoS_2 Heterojunctions. *ACS Nano* **2022**, *16* (7), 11036−11048.

(4) Duong, N. T.; Lee, J.; Bang, S.; Park, C.; Lim, S. C.; Jeong, M. S. Modulating the Functions of $MoS_2/MoTe_2$ van der Waals Heterostructure via Thickness Variation. *ACS Nano* **2019**, *13* (4), 4478−4485.

(5) Wu, E.; Xie, Y.; Liu, Q.; Hu, X.; Liu, J.; Zhang, D.; Zhou, C. Photoinduced Doping to Enable Tunable and High-Performance Anti-Ambipolar $MoTe_2/MoS_2$ Heterotransistors. *ACS Nano* **2019**, *13* (5), 5430−5438.

(6) Paul Inbaraj, C. R.; Mathew, R. J.; Ulaganathan, R. K.; Sankar, R.; Kataria, M.; Lin, H. Y.; Chen, Y.-T.; Hofmann, M.; Lee, C.-H.; Chen, Y.-F. A Bi-Anti-Ambipolar Field Effect Transistor. *ACS Nano* **2021**, *15* (5), 8686−8693.

(7) Chen, C.-F.; Yang, S.-H.; Lin, C.-Y.; Lee, M.-P.; Tsai, M.-Y.; Yang, F.-S.; Chang, Y.-M.; Li, M.; Lee, K.-C.; Ueno, K.; Shi, Y.; Lien, C.-H.; Wu, W.-W.; Chiu, P.-W.; Li, W.; Lo, S.-T.; Lin, Y.-F. Reversible Charge-Polarity Control for Multioperation-Mode Transistors Based on van der Waals Heterostructures. *Adv. Sci.* **2022**, *9* (24), No. 2106016.

(8) Pan, C.; Wang, C.-Y.; Liang, S.-J.; Wang, Y.; Cao, T.; Wang, P.; Wang, C.; Wang, S.; Cheng, B.; Gao, A.; Liu, E.; Watanabe, K.; Taniguchi, T.; Miao, F. Reconfigurable Logic and Neuromorphic Circuits Based on Electrically Tunable Two-Dimensional Homojunctions. *Nat. Electron.* **2020**, *3* (7), 383−390.

(9) Chen, Y.; Wang, Y.; Wang, Z.; Gu, Y.; Ye, Y.; Chai, X.; Ye, J.; Chen, Y.; Xie, R.; Zhou, Y.; Hu, Z.; Li, Q.; Zhang, L.; Wang, F.; Wang, P.; Miao, J.; Wang, J.; Chen, X.; Lu, W.; Zhou, P.; Hu, W. Unipolar Barrier Photodetectors Based on van der Waals Heterostructures. *Nat. Electron.* **2021**, *4* (5), 357−363.

(10) Yang, S.-J.; Choi, S.; Odongo Ngome, F. O.; Kim, K.-J.; Choi, S.-Y.; Kim, C.-J. All-Dry Transfer of Graphene Film by van der Waals Interactions. *Nano Lett.* **2019**, *19* (6), 3590−3596.

(11) Iwasaki, T.; Endo, K.; Watanabe, E.; Tsuya, D.; Morita, Y.; Nakaharai, S.; Noguchi, Y.; Wakayama, Y.; Watanabe, K.; Taniguchi, T.; Moriyama, S. Bubble-Free Transfer Technique for High-Quality Graphene/Hexagonal Boron Nitride van der Waals Heterostructures. *ACS Appl. Mater. Interfaces* **2020**, *12* (7), 8533−8538.

(12) Zhang, Z.; Zhang, B.; Wang, Y.; Wang, M.; Zhang, Y.; Li, H.; Zhang, J.; Song, A. Toward High-Peak-to-Valley-Ratio Graphene Resonant Tunneling Diodes. *Nano Lett.* **2023**, *23* (17), 8132−8139.

(13) Bian, Z.; Miao, J.; Zhao, Y.; Chai, Y. Strong Interlayer Interaction for Engineering Two-Dimensional Materials. *Acc. Mater. Res.* **2022**, *3* (12), 1220−1231.

(14) Zhang, B.; Zhang, Z.; Han, H.; Ling, H.; Zhang, X.; Wang, Y.; Wang, Q.; Li, H.; Zhang, Y.; Zhang, J.; Song, A. A Universal Approach to Determine the Atomic Layer Numbers in Two-Dimensional Materials Using Dark-Field Optical Contrast. *Nano Lett.* **2023**, *23* (19), 9170−9177.

(15) Wang, M.; Zheng, X.; Ye, X.; Liu, W.; Zhang, B.; Zhang, Z.; Zhai, R.; Ning, Y.; Li, H.; Song, A. High-Performance Photodetectors Based on Semiconducting Graphene Nanoribbons. *Nano Lett.* **2024**, *24* (1), 165−171.

(16) Zhao, W.; Ghorannevis, Z.; Chu, L.; Toh, M.; Kloc, C.; Tan, P.-H.; Eda, G. Evolution of Electronic Structure in Atomically Thin Sheets of WS$_2$ and WSe$_2$. *ACS Nano* **2013**, *7* (1), 791−797.

(17) Bu, T.; Duan, X.; Liu, C.; Su, W.; Hong, X.; Hong, R.; Zhou, X.; Liu, Y.; Fan, Z.; Zou, X.; Liao, L.; Liu, X. Electrically Dynamic Configurable WSe$_2$ Transistor and the Applications in Photodetector. *Adv. Funct. Mater.* **2023**, *33* (48), No. 2305490.

(18) Zhang, G.; Lu, G.; Li, X.; Mei, Z.; Liang, L.; Fan, S.; Li, Q.; Wei, Y. Reconfigurable Two-Dimensional Air-Gap Barristors. *ACS Nano* **2023**, *17* (5), 4564−4573.

(19) Shim, J.; Jo, S. H.; Kim, M.; Song, Y. J.; Kim, J.; Park, J. H. Light-Triggered Ternary Device and Inverter Based on Hetero-junction of van der Waals Materials. *ACS Nano* **2017**, *11* (6), 6319−6327.

(20) Mahajan, M.; Majumdar, K. Gate- and Light-Tunable Negative Differential Resistance with High Peak Current Density in 1T-TaS/2H-MoS$_2$ T-Junction. *ACS Nano* **2020**, *14* (6), 6803−6811.

(21) Li, Y. T.; Wang, Y.; Huang, L.; Wang, X. T.; Li, X. Y.; Deng, H. X.; Wei, Z. M.; Li, J. B. Anti-Ambipolar Field-Effect Transistors Based On Few-Layer 2D Transition Metal Dichalcogenides. *ACS Appl. Mater. Interfaces* **2016**, *8* (24), 15574−15581.

(22) Zubair, M.; Wang, H.; Zhao, Q.; Kang, M.; Xia, M.; Luo, M.; Dong, Y.; Duan, S.; Dai, F.; Wei, W.; Li, Y.; Wang, J.; Li, T.; Fang, Y.; Liu, Y.; Xie, R.; Fu, X.; Dong, L.; Miao, J. Gate-Tunable van der Waals Photodiodes with an Ultrahigh Peak-to-Valley Current Ratio. *Small* **2023**, *19* (29), No. 2300010.

(23) Kim, S.; Jung, S.; Kim, B.; Yoo, H. Pre-State-Dependent Ternary/Binary Logic Operation Obtained by Inkjet Printed Indium Oxide and Single-Walled Carbon Nanotube/Indium Oxide Hetero-junction-Based Transistors. *IEEE Electron Device Lett.* **2023**, *44* (2), 265−268.

(24) Zhu, Z.; Persson, A. E. O.; Wernersson, L.-E. Reconfigurable signal modulation in a ferroelectric tunnel field-effect transistor. *Nat. Commun.* **2023**, *14* (1), 2530.

(25) Hayakawa, R.; Takahashi, K.; Zhong, X.; Honma, K.; Panigrahi, D.; Aimi, J.; Kanai, K.; Wakayama, Y. Reconfigurable Logic-in-Memory Constructed Using an Organic Anti-ambipolar Transistor. *Nano Lett.* **2023**, *23* (17), 8339−8347.

(26) Zhang, X.; Liu, B.; Gao, L.; Yu, H.; Liu, X.; Du, J.; Xiao, J.; Liu, Y.; Gu, L.; Liao, Q.; Kang, Z.; Zhang, Z.; Zhang, Y. Near-Ideal van der Waals Rectifiers Based on All-Two-Dimensional Schottky Junctions. *Nat. Commun.* **2021**, *12* (1), 1522.

(27) Zhou, C.; Zhang, S.; Lv, Z.; Ma, Z.; Yu, C.; Feng, Z.; Chan, M. Self-driven WSe$_2$ Photodetectors Enabled with Asymmetrical Van Der Waals Contact Interfaces. *npj 2D Mater. Appl.* **2020**, *4* (1), 46.

(28) Dai, M.; Chen, H.; Feng, R.; Feng, W.; Hu, Y.; Yang, H.; Liu, G.; Chen, X.; Zhang, J.; Xu, C.-Y.; Hu, P. A Dual-Band Multilayer InSe Self-Powered Photodetector with High Performance Induced by Surface Plasmon Resonance and Asymmetric Schottky Junction. *ACS Nano* **2018**, *12* (8), 8739−8747.

(29) Dai, M.; Chen, H.; Wang, F.; Long, M.; Shang, H.; Hu, Y.; Li, W.; Ge, C.; Zhang, J.; Zhai, T.; Fu, Y.; Hu, P. Ultrafast and Sensitive Self-Powered Photodetector Featuring Self-Limited Depletion Region and Fully Depleted Channel with van der Waals Contacts. *ACS Nano* **2020**, *14* (7), 9098−9106.

(30) Auton, G.; Zhang, J.; Kumar, R. K.; Wang, H.; Zhang, X.; Wang, Q.; Hill, E.; Song, A. Graphene Ballistic Nano-Rectifier with Very High Responsivity. *Nat. Commun.* **2016**, *7*, 11670.

(31) Hao, X. J.; Yuan, R. Y.; Ji, T.; Guo, Y. Switch Effect for Spin-Valley Electrons in Monolayer WSe$_2$ Structures Subjected to Optical Field and Fermi Velocity Barrier. *J. Appl. Phys.* **2020**, *128*, No. 154303.

(32) Liu, Y.; Guo, J.; Zhu, E.; Liao, L.; Lee, S.-J.; Ding, M.; Shakir, I.; Gambin, V.; Huang, Y.; Duan, X. Approaching the Schottky−Mott Limit in van der Waals Metal−Semiconductor Junctions. *Nature* **2018**, *557* (7707), 696−700.

(33) Liu, W.; Kang, J.; Sarkar, D.; Khatami, Y.; Jena, D.; Banerjee, K. Role of Metal Contacts in Designing High-Performance Monolayer n-Type WSe$_2$ Field Effect Transistors. *Nano Lett.* **2013**, *13* (5), 1983−1990.

(34) Cheng, R.; Yin, L.; Wang, F.; Wang, Z.; Wang, J.; Wen, Y.; Huang, W.; Sendeku, M. G.; Feng, L.; Liu, Y.; He, J. Anti-Ambipolar Transport with Large Electrical Modulation in 2D Heterostructured Devices. *Adv. Mater.* **2019**, *31* (24), No. 1901144.

(35) Gan, Y.; Qin, S.; Du, Q.; Zhang, Y.; Zhao, J.; Li, M.; Wang, A.; Liu, Y.; Li, S.; Dong, R.; Zhang, L.; Chen, X.; Liu, C.; Wang, W.; Wang, F. Ultrafast and Sensitive Self-Powered Photodetector Based on Graphene/Pentacene Single Crystal Heterostructure with Weak Light Detection Capacity. *Adv. Sci.* **2022**, *9* (35), No. 2204332.

(36) Dong, K.; Zhou, H.; Gao, Z.; Xu, M.; Zhang, L.; Zhou, S.; Cui, H.; Wang, S.; Tao, C.; Ke, W.; Yao, F.; Fang, G. 2D Perovskite Single-Crystalline Photodetector with Large Linear Dynamic Range for UV Weak-Light Imaging. *Adv. Funct. Mater.* **2024**, *34* (1), No. 2306941.

(37) Li, Y.; Zhou, J.; Tian, Y.; Wei, Z.; Shen, G. 2D Ruddlesden-Popper Sn-Based Perovskite Weak Light Detector for Image Transmission and Reflection Imaging. *Small Methods* **2024**, *8* (2), No. 2300026.

(38) Tang, Y.; Jin, P.; Wang, Y.; Li, D.; Chen, Y.; Ran, P.; Fan, W.; Liang, K.; Ren, H.; Xu, X.; Wang, R.; Yang, Y.; Zhu, B. Enabling Low-Drift Flexible Perovskite Photodetectors by Electrical Modulation for Wearable Health Monitoring and Weak Light Imaging. *Nat. Commun.* **2023**, *14* (1), 4961.

(39) Hao, D.; Liu, D.; Shen, Y.; Shi, Q.; Huang, J. Air-Stable Self-Powered Photodetectors Based on Lead-Free CsBi$_3$I$_{10}$/SnO$_2$ Heterojunction for Weak Light Detection. *Adv. Funct. Mater.* **2021**, *31* (21), No. 2100773.

(40) Guo, L.; Zhang, K.; Tao, M.; Zhao, R.; Wu, T.; Wang, Y.; Song, Y. Bio-Inspired Micro Area Concentrated Array Assisted Perovskite Photodetector toward Weak Light Imaging. *J. Mater. Chem. C* **2023**, *11* (24), 8045−8051.

(41) Xing, R.; Shi, P.; Wang, D.; Wu, Z.; Ge, Y.; Xing, Y.; Wei, L.; Yan, S.; Tian, Y.; Bai, L.; Chen, Y. Flexible Self-Powered Weak Light Detectors Based on ZnO/CsPbBr$_3$/γ-CuI Heterojunctions. *ACS Appl. Mater. Interfaces* **2022**, *14* (35), 40093−40101.

(42) Li, P.; Huang, W.; Xu, W.; Wei, X.; Chen, Y.; Meng, F.; Deng, W.; Liu, J. In Situ Polymer-Imprinted Architecture of Textured Perovskite Single-Crystal Sheets for Ultraweak-Light Photodetection. *Adv. Opt. Mater.* **2023**, *11* (4), No. 2201876.

(43) Lin, X.; Deng, H.; Jia, Y.; Wu, Z.; Xia, Y.; Wang, X.; Chen, S.; Cheng, Y.; Zheng, Q.; Lai, Y.; Cheng, S. Self-Powered Sb$_2$S$_3$ Thin-Film Photodetectors with High Detectivity for Weak Light Signal Detection. *ACS Appl. Mater. Interfaces* **2022**, *14* (10), 12385−12394.